Cement and Concrete Composites 105 (2020) 103439

Contents lists available at ScienceDirect

Cement and Concrete Composites

journal homepage: http://www.elsevier.com/locate/cemconcomp

Predicting effective thermal and elastic properties of cementitious composites containing polydispersed hollow and core-shell micro-particles

Zhenglai Shen, Hongyu Zhou *

Department of Civil and Environmental Engineering, University of Tennessee, Knoxville, TN, 37996, USA

ARTICLE INFO

Keywords:
Predictive model
Functional cementitious composites
Core-shell particle

ABSTRACT

Micro- and nano-sized hollow and core-shell particles (CSPs) have attracted tremendous interests in developing functional cementitious composites and concretes. In this paper, a general method is developed to predict the thermal and elastic properties of cementitious composites containing core-shell and hollow micro-particles. The model follows a two-stage homogenization process – CSP inclusions together with their surrounding interfacial transition zone (ITZ) are first treated as equivalent solid particles, and then the homogenized properties of the composite system are obtained using numerical (i.e., finite element) or analytical (Mori-Tanaka) approaches. Compared with other homogenization methods, the proposed model is easy-to-use and versatile. The numerical model, validated by experimental results, is then used to guide the design of functional cementitious composites. The results show that CSP particle size (or relative shell thickness), volume fraction, shell property, and the size of the ITZ have significant impacts on the effective thermal and elastic properties of cementitious composites; whereas the particle size distribution pattern has relatively minor influence. In addition, the effective property of the composite is more sensitive to the particle property change when CSP inclusions are much stiffer or more thermally conductive than the matrix. Lastly, a scoping study is conducted to elucidate the relationship between the effective thermal conductivity and effective elastic moduli for cementitious composites containing CSP additives with different shell materials, particle sizes, and volume concentrations etc.

1. Introduction

In the past decade, micro- and nano-sized core-shell particles (CSPs) have been increasingly studied for functional cementitious composites and concretes. For example, hollow fly-ash cenosphere (FAC) and hollow glass microspheres (HGM) have been used to develop lightweight and ultra-lightweight cementitious composites (LCC/ULCC) [1–5], where polydispersed FAC and HGM particles with particle size ranging from a few microns to 1 mm are mixed into cementitious matrix to form cellular solids. The particles are typically hollow with a nearly 70–90 vol % air core and a thin rigid shell. LCC/ULCC made with hollow FACs and HGMs have much higher strength-to-density ratio and stiffness than conventional lightweight aggregate and aerated concretes, and thus, have the potential to be used in load-bearing structural components [1,2]. In addition, CSPs have been explored as support/packaging materials for functional additives and catalysts in cementitious composites. For example, microencapsulated phase-changing materials (PCMs) have been mixed into cement mortar/concrete for saving building operational energy [6,7]. In such applications, organic PCMs (e.g., paraffin wax) are typically encapsulated in microcapsules with a mediam diameter of 1 to a few hundred microns and a capsule thickness of a few microns, to prevent the leakage of liquid PCM and the reaction with the cementitious matrix [6,7]. Other applications of CSP in cementitious materials include self-healing concretes that contain microcapsules filled with healing agents such as mineral compounds and bacteria. The healing agents are encapsulated within thin polymeric shells, such as poly (phenol–formaldehyde) (PF), to produce additives that are readily mixed with other ingradients of concrete [8,9]. When the polymeric capsules are ruptured by a propagating stress crack, the encapsulated healing agent is released to seal the crack [8].

For materials that are used as thermal insulation or when the cooling/heating rate is critical for their functionality (e.g., thermally insulating concrete, or cementitious composites containing PCMs), the heat transfer in cementitious material containing CSP is of great interest [2,10]. Moreover, when the mechanical properties (e.g., elastic modulus and strength) of the encapsulation materials and the encapsulated functional core (e.g., air, PCM) are inferior to the cementitious matrix, the inclusion of CSPs into cementitious matrix could result in substantial

* Corresponding author. 851 Neyland Drive, 325 John D. Tickle Building, Knoxville, TN, 37996-2313, USA.
E-mail address: hzhou8@utk.edu (H. Zhou).

https://doi.org/10.1016/j.cemconcomp.2019.103439
Received 7 December 2018; Received in revised form 25 July 2019; Accepted 23 October 2019
Available online 2 November 2019

degradation of mechanical properties [11,12]. Whereas studies indicated that using rigid shell encapsulation materials such as FAC may circumvent the strength and stiffness loss [4,5,13]. Thus, for functional cementitious composites that also bear mechanical stress, it is essential to understand how the inclusion of CSPs would influence their mechanical properties.

The thermal and mechanical properties of functional cementitious composites and concretes depend largely on their hierarchical microstructure [14], see Fig. 1. At the cement paste level, both unreacted species and hydration products are present and agglomerated by an amorphous product, C–S–H gel. The properties of hardened cement paste are dictated by the relative amount and distribution of C–S–H and inclusions of anhydrous, portlandite, ettringite, and capillary pores [15]. For cementitious composites, a single CSP is typically comprised of a functional core (air, PCM, or other functional agents) and a soft (e.g., polymers) or rigid (e.g., glass or ceramic) shell interacting with the surrounding cementitious matrix. Since most CSP shells are not reactive to cement, an interfacial transition zone (ITZ) is developed between the surface of CSP inclusions and the cementitious matrix [16]. The ITZ within cementitious composites containing micro-sized CSP inclusions may have substantial accumulative impacts on the material's thermal and mechanical properties – i.e., due to the small particle size of most micro-CSP inclusions, their total surface area is typically large; secondly, the thickness of ITZ around micro-size inclusions may be comparable to their particle size, although few studies have been conducted on micron- and sub-micron size inclusions [12]. At mesoscale (i.e., dimension from a few hundred microns to millimeters range), the entrapped air bubbles, fine and coarse aggregates are incorporated as if the cementitious matrix containing micro-CSP is a homogenized medium [14], and the two-phase models (or three-phase models to account for ITZ) generally have sufficient accuracy for the materials' property predictions [12,17]. The prediction of the effective properties of a heterogeneous material typically assumes that the problem contains two or more scales which are well separated – i.e., the microscopic scale (microstructure of cement paste) is small enough for the heterogeneities to be smeared out in the next scale level computation, see Fig. 1 (b). In this paper, our discussion focuses on the composite level (i.e., the shaded boxes shown in Fig. 1 (b)), particularly, the treatment of CSP particles and the surrounding ITZ, as well as the homogenization method to obtain the elastic and thermal conductive properties of cementitious composites containing micro-size CSP inclusions.

2. Background

Since Eshelby's pioneer work on the elastic solution of a single inclusion embedded in an infinite medium [18], there have been a variety of effective medium theory models developed for studying the elastic and thermal properties of composite systems. Hill first applied the self-consistent method to calculate the effective elastic properties of polycrystalline metals. The self-consistency method postulates that the orientation average of the stress or strain within the inclusion phase is equal to the overall stress or strain of the effective medium. The resultant effective property is an implicit tensor formula [19]. Christensen combined the self-consistent method with the composite spheres model proposed by Hashin [20] and developed a well-known three-phase model or the generalized self-consistent model (GSCM), which consists a single composite sphere embedded in the infinite medium of unknown effective property [21]. As compared to the self-consistency method develop by Hill, the generalized self-consistent method can better account for the matrix-inclusion interactions [22]. McLaughlin applied a differential scheme in an effective medium approach and developed the differential effective medium theory (DEMT) [23]. It approximates the effective properties of the composites incrementally through a process of homogenization, with the added inclusion always in a diluted suspension and the matrix phase takes the properties of the existing composite material from the previous homogenization step. Following the DEMT, a generalized differential effective medium theory was developed by Norris et al. [24], assuming that the homogenization process is path-dependent, i.e., the effective properties depend upon the way in which the final composite material was constructed from an initially homogeneous material.

On the other hand, Mori and Tanaka [25] introduced the concept of mean stress in the matrix and derived for its volume-concentration dependence when the inclusion regions possess a certain amount of

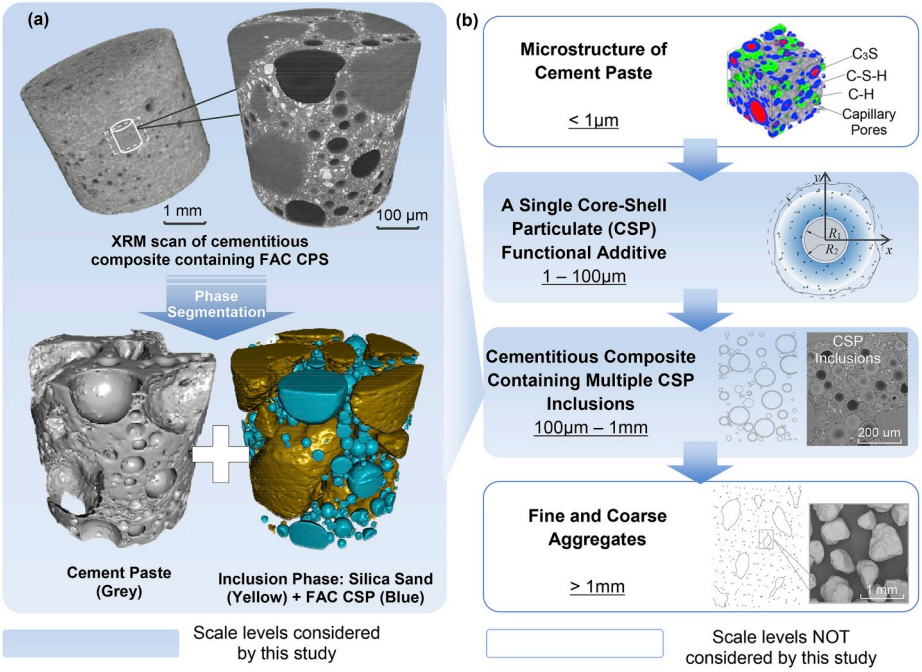

Fig. 1. The hierarchical microstructure of cementitious composite materials containing core-shell particulate fillers: (a) X-ray micro-tomography (XRM) and 3D reconstruction of the cementitious matrix and the inclusion phases; and (b) the different scales involved in a functional cementitious composite (shaded blocks are considered in this study).

transformation strain. This method, which is generally referred to as the Mori-Tanaka method, has been subsequently developed into various forms [26] with successful applications in predicting the elastic and thermoelastic behavior of composite materials [27]. In comparison with some other effective medium theories, the Mori-Tanaka method delivers explicit close-form solutions for both effective elastic moduli and effective thermal conductive properties; in addition, the derived effective properties always coincide or lie within the well-established Hashin-Shtrikman bounds [27,28]. For cementitious materials, different variations of the Mori-Tanaka method have been applied for property estimations. For example, Silva et al. [29] and Constantinides and Ulm [30] applied Mori-Tanaka method to predict the elastic properties of cementitious composited based on nanoindentation measurements. The Mori-Tanaka method has also been applied to study the effective elastic properties of self-healing cementitious materials [31] and lightweight aggregate concrete [32]. In addition, the Mori-Tanaka method has been applied to evaluate the effective thermal conductivity of foam concrete [33] and cementitious composites with phase change materials [34,35]. Although the Mori-Tanaka approach takes into account the stress perturbation inside the matrix due to the presence of other inclusions, it is not able to account for the spatial distribution. Therefore, numerical homogenization such as finite element approach has been applied for composite systems having higher geometric complexities [36,37].

In this paper, a general method to predict the thermal and elastic properties of cementitious composites containing core-shell and hollow micro-particles is introduced following a two-stage homogenization process: first, the elastic and thermal properties of the hollow/core-shell particular inclusions are equivalently represented by solid particles of the same size. The effect of the interfacial transition zone (ITZ) with varying properties around each inclusion is considered. Then, the effective properties of cementitious composites are obtained following a differential scheme by using either the Mori-Tanaka method or microstructure-guided finite element analysis (FEA). The theoretical and numerical models are validated by experimental test results and then used to study the effects of sphere size, ITZ size (and property distribution), and shell properties to provide guidelines for the design of micro-size core-shell particulate additives for cementitious composite materials. Furthermore, the effects of CSP size distribution, volume concentration, and particle shapes are also investigated. Finally, the relationship between the effective thermal conductivity and the effective elastic moduli is plotted in a material property chart to examine the design space of cementitious composites containing hollow or core-shell functional additives. Since hollow particles belong to a special type of core-shell particle with the inner core filled with air, they are both interchangeably referred as to CPS for this discussion.

3. Effective thermal and elastic properties prediction

The two-stage homogenization process adopted in this study is illustrated by Fig. 2, where Stage 1 computes the equivalent elastic and thermal conductive properties of a core-shell particle into an equivalent solid sphere of the same size (volume). The influence of interfaces between the inner core and shell as well as the interfacial transition zone (ITZ) is accounted for by following a two-step equivalence scheme shown in Fig. 3. Once the equivalent properties of individual inclusions, which is size-dependent – i.e., the equivalent elastic and thermal properties of a CSP are functions of its size, shell thickness etc., Stage 2 computes the homogenized properties of the composite system following a differential scheme, where numerical (e.g., finite element) or analytical (e.g., Mori-Tanaka) homogenization methods are used. Details of the two-stage homogenization process for cementitious composites containing CSP are introduced as follows.

3.1. Equivalence between a hollow/core-shell particle and a solid particle

Fig. 3 schematically shows the equivalence between a CSP and an equivalent solid particle, including the consideration of the interfacial transition zone (ITZ) with varying material properties (i.e., due to wall effect of the inclusion).

The equivalence of elastic properties between a core-shell inclusion and a solid particle can be established through Eshelby's strain energy equivalence [38], where the equivalent bulk modulus of the inclusion, K_I^{eq}, is obtained as [21]:

$$K_I^{eq} = K_s + \frac{(K_c - K_s)p}{1 + (1-p)\left[(K_c - K_s)\Big/\left(K_s + 4/3\mu_s\right)\right]} \tag{1}$$

where $p = (R_1/R_2)^3$ is the volumetric ratio of the core in a CSP, see Fig. 3; K_s, μ_s, and K_c, μ_c are the bulk and shear moduli of the shell and core

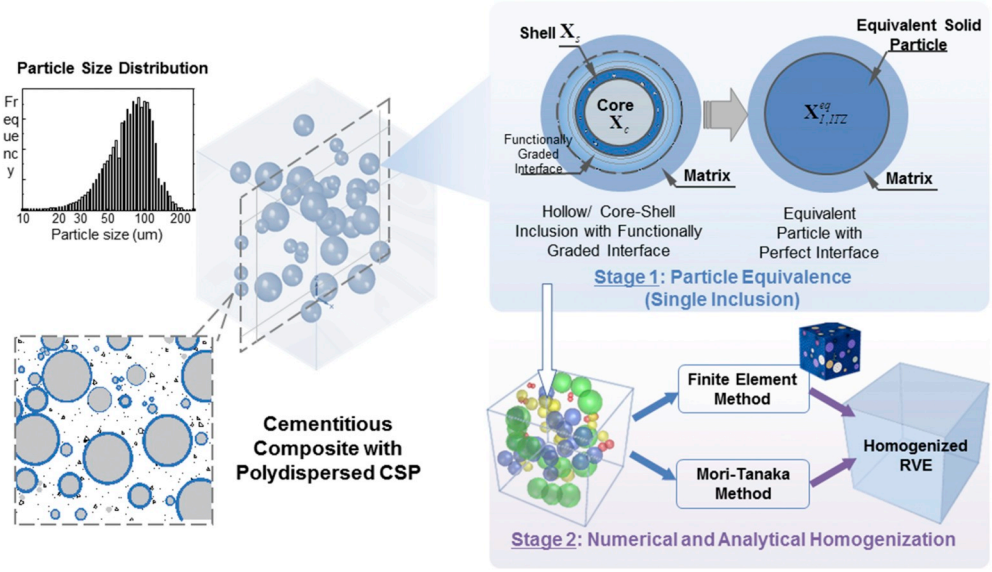

Fig. 2. The two-stage homogenization process to obtain thermal and elastic properties of cementitious composite materials containing hollow/core-shell particulate additives.

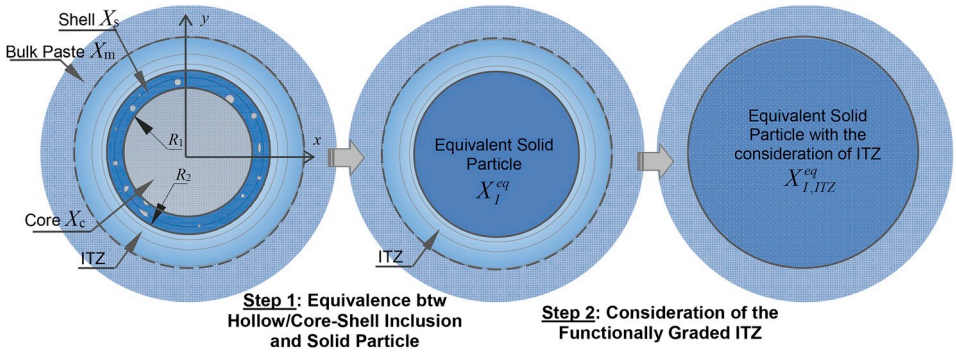

Fig. 3. Equivalence between a hollow/core-shell particle and a solid particle.

materials, respectively.

The equivalent shear modulus of a hollow inclusionμ_I^{eq}, is obtained by solving:

$$A_1\left(\frac{\mu_I^{eq}}{\mu_s}\right)^2 + A_2\left(\frac{\mu_I^{eq}}{\mu_s}\right) + A_3 = 0 \tag{2}$$

where

$$A_1 = 8z[9(K_s+2\mu_s)/2(3K_s+\mu_s)]\eta_1 p^{10/3} - 2[63z\eta_2 + 2\eta_1\eta_3]p^{7/3} + 252z\eta_2 p^{5/3} - 25z\left[9\left(3K_s^2+4K_s\mu_s+3\mu_s^2\right)/(3K_s+\mu_s)^2\right]\eta_2 p + [4(6K_s+17\mu_s)/(3K_s+\mu_s)]\eta_2\eta_3 \tag{3a}$$

$$A_2 = 6z[(3K_s-4\mu_s)/(3K_s+\mu_s)]\eta_1 p^{10/3} + 4(63z\eta_2+2\eta_1\eta_3)p^{7/3} - 504z\eta_2 p^{5/3} + 75z\left[\left(45K_s^2/2 - 3K_s\mu_s - 8\mu_s^2\right)/(3K_s+\mu_s)^2\right]\eta_2 p + [3(3K_s-44\mu_s)/2(3K_s+\mu_s)]\eta_2\eta_3 \tag{3b}$$

$$A_3 = -6z[(9K_s+8\mu_s)/(3K_s+\mu_s)]\eta_1 p^{10/3} - 2(63z\eta_2+2\eta_1\eta_3)p^{7/3} + 252z\eta_2 p^{5/3} + 25z\left[(3K_s-2\mu_s)^2/4(3K_s+\mu_s)^2 - 7\right]\eta_2 p - [(57K_s+4\mu_s)/2(3K_s+\mu_s)]\eta_2\eta_3 \tag{3c}$$

with $z = \mu_c/\mu_s - 1$, and

$$\eta_1 = [(57K_c+4\mu_c)(6K_s+17\mu_s)(\mu_c/\mu_s) - (6K_c+17\mu_c)(57K_s+4\mu_s)] / 2(3K_c+\mu_c)(3K_s+\mu_s)$$

$$\eta_2 = [(57K_c+4\mu_c)(\mu_c/\mu_s) + 12(9K_c+8\mu_c)] / 2(3K_c+\mu_c)$$

$$\eta_3 = [18(K_s+2\mu_s)(\mu_c/\mu_s) + 3(9K_s+8\mu_s)] / 2(3K_s+\mu_s)$$

The equivalent thermal conductivity of the inclusion, χ_I^{eq}, with the consideration of contact resistance between the core and shell can be obtained through effective medium theory as:

$$\chi_I^{eq} = \frac{2(1-f)\chi_s\chi_c + (2(1-f)\chi_s + (1+2f)\chi_c)(R_1/h_{cs})}{(2+f)\chi_s\chi_c + ((2+f)\chi_s + (1-f)\chi_c)(R_1/h_{cs})}\chi_s \tag{4}$$

where χ_c and χ_s are the thermal conductivities of the core and shell, respectively; and $f = \left(1+\frac{t_s}{R_1}\right)^{-3}$, $t_s = R_2 - R_1$ is the thickness of the shell, R_1 is the radius of the core, h_{cs} is the contact resistance at the interface between the core and shell of the core/shell particle. The deduction of Equation (4) is provided in Appendix A.

For ideal contact, i.e., $h_{cs}\to 0$, the equivalent thermal conductivity of the inclusion simply reduce to Ref. [39]:

$$\chi_I^{eq} = \frac{2(1-f)\chi_s + (1+2f)\chi_c}{(2+f)\chi_s + (1-f)\chi_c}\chi_s \tag{5}$$

3.2. Consideration of interfacial transition zone (ITZ) with variable properties

It is well recognized that the wall effect of aggregate/inclusions in cementitious composites leads to an initial cement gradient within the interfacial transition zone (ITZ) [40]. For cementitious composites containing micro-/or even nano-size functional inclusions, the size of the ITZ, albeit small, may be comparable to the particle size [12,41,42]. The ITZs, in this case, have a substantial impact on both the effective elastic and conductive properties of the composites [12]. In this study, a layer of ITZ surrounding the CSP inclusions was considered as part of an "effective particle," see Fig. 3. Due to the effect of the inclusion surface on the distribution of cement grains, an initial cement gradient is formed at the ITZ. Although available experimental data on ITZ properties are insufficient to formulate precisely the law of variation of the interface properties across the thickness [40], many existing research indicated that the elastic stiffness of ITZ layers within cementitious composites is substantially lower than that of the bulk matrix because of its higher porosity and that this change is smooth with "upward convexity'' (Fig. 4 (a)), where a power law may be applied to describe the property variation within ITZ regions [43].

3.2.1. Consideration of ITZ with graded properties

To find the elastic and thermal conductive constants of the equivalent homogeneous particle that has the radius of the CSP inclusion plus the interphase thickness and that produces the same effect on the overall property as CSP inclusion with an interphase layer having variable properties, the method proposed by Shen and Li [44,45] is adapted herein, which applies the Mori-Tanaka method: the equivalent properties of the CSP inclusion including the interface layer, $X_{I,ITZ}^{eq}$, can be obtained by considering a certain 'current' radius, R ($R_2 < R < R_3$), and then an incremental layer dR of the interphase material is added, $R + dR$, see Fig. 4 (a). Assuming that the inclusion of radius R is homogeneous (homogenized at the previous step), the corresponding increment $X_{I,ITZ}^{eq}$ is obtained by placing the inclusion of radius R into a matrix that has the property of the interface $X_{ITZ}(R)$. Volume fraction of the homogenized inclusion in the matrix, φ_I, is the ratio of the volume of the inclusion of radius R to the volume of the enlarged inclusion of radius $R + dR$, and

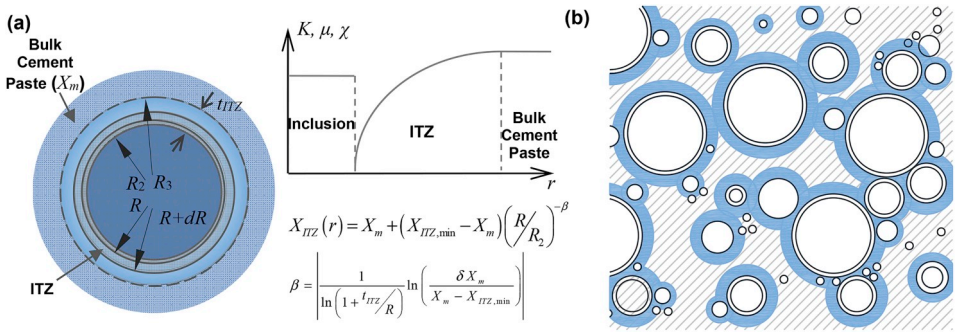

Fig. 4. Consideration of the interfacial transition zone (ITZ): (a) ITZ around a single inclusion; (b) illustrative figure showing the ITZ percolation (connectivity), not to-scale.

when dR is small $\varphi_I \rightarrow 1 - 3dR/R$. Shen and Li [44,45] treat this system as a composite, and apply the Mori-Tanaka method:

$$\frac{dX_{I,ITZ}^{eq}(R)}{dR} = -\frac{3}{R}\frac{\left(X_{I,ITZ}^{eq}(R) - X_{ITZ}(R)\right)}{\Gamma_{dil}^{X}} \tag{6}$$

where, Γ_{dil}^{X} is the dilute concentration factor.

If the elastic and conductive constants are assumed to follow the power law variation across the interphase thickness, we have [43]:

$$X_{ITZ}(R) = X_m + (X_{ITZ,\min} - X_m)\left(R/R_2\right)^{-\beta}, \quad R_2 < R < R_2 + t_{ITZ} \tag{7}$$

where $X_{ITZ,\min}$ is the minimum value across the ITZ region (at the particle boundary, see Fig. 4 (a)) and the power exponent is:

$$\beta = \left| \frac{1}{\ln\left(1 + t_{ITZ}/R\right)} \ln\left(\frac{\delta X_m}{X_m - X_{ITZ,\min}}\right) \right| \tag{8}$$

where t_{ITZ} is the thickness of interface layer; and δ is normally chosen as a small value such that the ITZ properties are continuous at the inner boundary and are almost matched to the matrix values at the outer boundary [43].

3.2.2. Percolation (connectivity) of ITZ region

As the volume fraction of the inclusion phase increases, the interfacial transition zones may start to overlap (percolate), see Fig. 4 (b). The overlap and connectivity of ITZ may influence the material's mechanical and thermal properties greatly, especially when the particle volume fraction is high. In this study, the ITZ percolation is accounted for by using the 'void exclusion probability', $e_V(t_{ITZ})$, defined by Lu and Torquato [46] where the volume fraction of ITZ, φ_{ITZ}, considering ITZ overlap, is calculated as [16,47]:

$$\varphi_{ITZ} = 1 - \varphi - e_V(t_{ITZ}) \tag{9}$$

where φ is the volume fraction of inclusions; and the evaluation of $e_V(t_{ITZ})$ can be found in Refs. [16,47].

3.3. Homogenization for effective properties

Once the equivalent properties are obtained for each core-shell particle, the homogenization process (Stage 2) can be performed using either numerical or analytical homogenization methods.

3.3.1. Homogenization using finite element method

A microstructure-guided finite element method (FEM) [14,37,48] can be used to compute the homogenized properties of cementitious

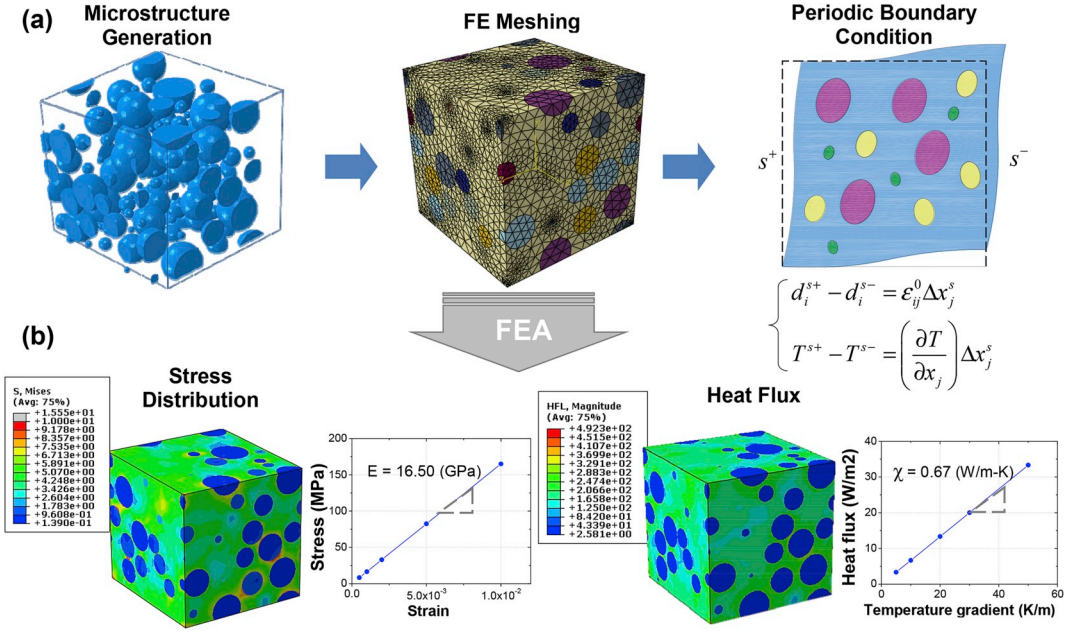

Fig. 5. Microstructure-guided FEA procedures: (a) microstructure generation, meshing, and applying periodic boundary condition; and (b) post-processing: stress and heat flux distributions and the determination of the effective elastic modulus and thermal conductivity of RVE.

composites containing core-shell particles. For a single representative volume element (RVE) within the composite system, the polydispersed spherical CSPs are simulated using the random packing algorithm developed by Lubachevsky and Stillinger [49]. The Lubachevsky and Stillinger approach employs non-overlapping particles on a cubical RVE. Specifically, a representative number of particles having null volume are created in the RVE domain. Then, a random velocity vector and a radius growth rate are assigned to each particle, where the growth rates assigned to particles are governed by the particle size distribution. During the iterative growing process, particle contacts are checked and the post-contact velocities are updated until the prescribed inclusion volume fraction is attained, see Fig. 5 (a).

Once the RVE microstructure is generated, periodic boundary conditions are applied to the RVE to ensure the assembly of individual RVE is a continuous body [50]. For the calculation of elastic properties, the displacement field of the two opposite parallel surfaces are constrained through [37]:

$$d_i^{s+} - d_i^{s-} = \varepsilon_{ij}^0 \Delta x_j^s \tag{10}$$

where, d_i^{s+} and d_i^{s-} are the displacement on the s^+ and s^- surfaces in the i-th direction ($i = x_1, x_2, x_3$) respectively; $\varepsilon_{ij}^0 \Delta x_j^s$ is the applied displacement boundary condition, ε_{ij}^0 is a constant strain and $\Delta x_j^s = x_j^{s+} - x_j^{s-}$ is the unit cell length.

Whereas for heat conduction, the periodic boundary condition on the pair of two opposite parallel boundary surfaces is [48]:

$$T^{s+} - T^{s-} = \left(\frac{\partial T}{\partial x_j}\right) \Delta x_j^s \tag{11}$$

where T^{s+} and T^{s-} are the temperature on the s^+ and s^- surfaces respectively; $\left(\frac{\partial T}{\partial x_j}\right)\Delta x_j^s$ is the applied temperature difference at boundaries.

The RVE is then meshed and the FE analysis is carried out using a FE solver (i.e., ABAQUS). To obtain the effective elastic and thermal properties of the RVE, a Python script is implemented to obtain effective volume-averaged RVE stresses, strains and heat flux, see Fig. 5 (b). The volumetric average effective elastic property and thermal conductivity are thereby obtained by correlating the applied strain (temperature gradient) and the corresponding average stress (heat flux).

3.3.2. Mori-Tanaka approach

Alternatively, the analytical homogenization can be carried out using the Mori-Tanaka method [51] where for the elastic properties the effective elastic tensor, $\overline{\mathbf{C}}$, of a composite system containing N inclusions (the ith) may be estimated as:

$$\overline{\mathbf{C}} = \mathbf{C}_m + \sum_{i=1}^{N} \varphi_i (\mathbf{C}_{I,i} - \mathbf{C}_m) \mathbf{\Gamma}^{\mathrm{C}}_{(\mathrm{MT}),i} \tag{12}$$

where φ_i is the volume fraction of the ith inclusion; $\mathbf{C}_{I,i}$ and $\mathbf{C}_m$ are the elastic tensors of the ith inclusion and the matrix, respectively; and $\mathbf{\Gamma}^{\mathrm{C}}_{(\mathrm{MT}),i}$ is the Mori-Tanaka strain concentration tensor of the ith inclusion:

$$\mathbf{\Gamma}^{\mathrm{C}}_{(\mathrm{MT}),i} = \left[\varphi_i \mathbf{I} + \varphi_m \left(\mathbf{\Gamma}^{\mathrm{C}}_{dil,i}\right)^{-1} + \sum_{j=1}^{N} \varphi_j \mathbf{\Gamma}^{\mathrm{C}}_{dil,j} \left(\mathbf{\Gamma}^{\mathrm{C}}_{dil,i}\right)^{-1}\right]^{-1}, \quad j \neq i \tag{13}$$

where $\mathbf{I}$ is a fourth order identity tensor, φ_m is the volume fraction of the matrix, and $\mathbf{\Gamma}^{\mathrm{C}}_{dil,i}$ is the strain concentration tensor of the ith inclusion under dilute scheme [51]:

$$\Gamma^{\mathrm{C}}_{\mathrm{dil,i}} = \left[\mathrm{I} + \mathrm{S}^{\mathrm{C}}_{\mathrm{m}} \mathrm{C}^{-1}_{\mathrm{m}} (\mathrm{C}_{\mathrm{I,i}} - \mathrm{C}_{\mathrm{m}})\right]^{-1} \tag{14}$$

$\mathbf{S}^{\mathrm{C}}_m$ is the Eshelby's tensor, which can be found in Ref. [18].

Similarly, for the effective thermal conductivity tensor, $\overline{\boldsymbol{\chi}}$:

$$\overline{\boldsymbol{\chi}} = \boldsymbol{\chi}_m + \sum_{i=1}^{N} \varphi_i (\boldsymbol{\chi}_{I,i} - \boldsymbol{\chi}_m) \mathbf{\Gamma}^{\chi}_{(\mathrm{MT}),i} \tag{15}$$

where $\boldsymbol{\chi}_{I,i}$, $\boldsymbol{\chi}_m$ are the thermal conductivity tensor of the ith inclusion and matrix respectively, and $\mathbf{\Gamma}^{\chi}_{(\mathrm{MT}),i}$ is the temperature gradient concentration tensor [52].

Note that Equation (12) and Equation (15) take the same form, thus, for the convenience of this discussion Equations (12) and (15) are generically written as:

$$\overline{\mathbf{X}} = \mathbf{X}_m + \sum_{i=1}^{N} \varphi_i (\mathbf{X}_{I,i} - \mathbf{X}_m) \mathbf{\Gamma}^{X}_{(\mathrm{MT}),i} \tag{16}$$

where $\mathbf{X}$ denotes the elastic or thermal conductive constants as the case applies.

4. Materials and experimental methods

To validate the model formulated in the previous section, cement paste samples containing four different types of solid and hollow microspheres were made using an ASTM C150 compliant Type I/II ordinary portland cement (OPC). Three types of hollow glass microsphere (HGM) bubbles (K25 and S60 manufactured by 3M™, and 110P8 manufactured by Potters Industries LLC) were used as micro-sized hollow inclusions, and one type of solid glass beads (SGB) (A3000 manufactured by Potters Industries LLC) was used as a stiff inclusion. A *Horiba LA-950* static light scattering particle size analyzer was used to determine the particle size distributions of the particulate inclusions and the results are plotted in Fig. 6 (a). The shell thicknesses of hollow particles were measured using scanning electron microscopy (SEM) imaging where the particles were embedded in epoxy and ground/polished to expose the section of the particle shell. The cementitious composites used for experimental testing were prepared according to ASTM C305 specifications. All mixtures were prepared at a fixed water-to-cement ratio, w/c = 0.28. The CSP inclusions were added at volume fractions of 7.5%, 15%, 30%, and 45%. A high range water-reducer was used to enhance the followability of the mixtures.

The modulus of elasticity was measured using a 10 kN *MTS Insight* electromechanical servo test machine according to ASTM C469 specifications, see Fig. 6 (b). Five 50 mm diameter by 100 mm height cylinders were made and tested for each specimen group, and the mechanical loading was carried out in a displacement-control mode with the loading rate of 0.05 mm/min. The average strain was measured using a pair of clamp-on extensometers (*Epsilon Tech*) with a gauge length of 50 mm, see Fig. 6 (b). The thermal conductivity and thermal diffusivity were tested through the transient plane source (TPS) method [53] using a *HotDisk TPS-1500* thermal constant analyzer [54], see Fig. 6 (c). In a TPS test, the transient temperature rise of a plane source (i.e., a Kapton supported double spiraled nickel metal sensor, see Fig. 6 (c)) that heats the surrounding material is measured. By measuring the unbalanced voltage drop as the function of time, the thermal conductivity, χ, and thermal diffusivity, κ, of the tested material are solved from one single transient recording through a process of iteration [55]. For the thermal conductivity measurements, three pairs of disc-shape cement mortar samples (50 mm diameter and 20 mm thick) were used. Before testing, all samples were dried in a convection oven for 48 h and cooled down to room temperature in an air-tight desiccant cabinet to prevent surface condensation. The particle properties, together with the measured elastic modulus and thermal constants are listed in Table 1.

5. Results and discussion

5.1. The equivalence between hollow/core-shell sphere and solid particles

We first discuss the equivalence between a core-shell or hollow

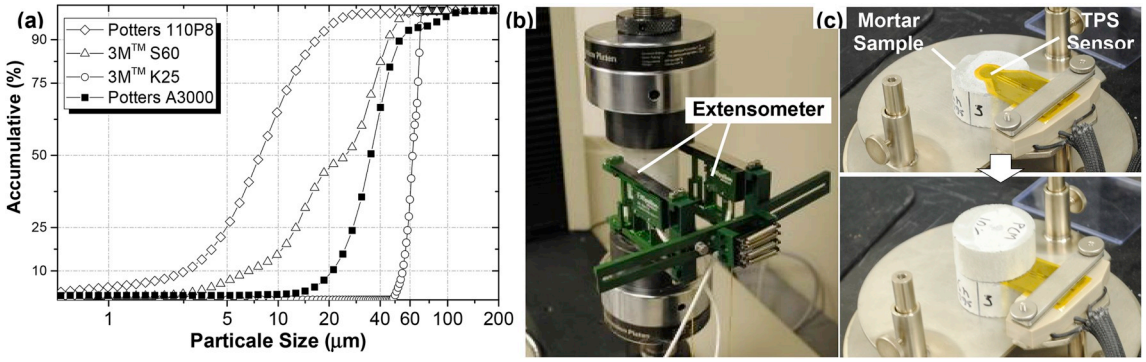

Fig. 6. (a) Particle size distribution of the CSP inclusions; and experimental test setup for (b) elastic modulus measurement; and (c) thermal conductivity measurement using Transient Plane Source (TPS) method.

Table 1
CSP properties used in the experimental and test results.

Group ID	CSP type	t_s[a]	Particle size			$2t_s/D_{50}$	CSP Volume Fraction, ϕ	Elastic Modulus[b]	Thermal Conductivity
			D_{10}	D_{50}	D_{90}				
		μm	μm				%	GPa	W/mK
Ref	–	–		–		–	0	23.96 ± 0.55	0.926 ± 0.019
A3000-075	Potter A3000 (solid)	–	20.9	35.2	52.8	–	7.5	25.44 ± 0.36	0.907 ± 0.009
A3000-150							15	25.89 ± 0.26	0.890 ± 0.015
A3000-300							30	27.46 ± 0.11	0.875 ± 0.005
A3000-450							45	29.30 ± 0.42	0.851 ± 0.002
K25-075	3 M K25	0.69	9.0	24.2	55.2	0.055	7.5	20.81 ± 0.20	0.817 ± 0.009
K25-150							15	19.08 ± 0.17	0.760 ± 0.005
K25-300							30	15.20 ± 0.33	0.617 ± 0.005
K25-450							45	12.35 ± 0.08	0.488 ± 0.010
S60-075	3 M S60	1.32	6.8	25.0	44.7	0.105	7.5	21.21 ± 0.41	0.841 ± 0.010
S60-150							15	19.84 ± 0.35	0.781 ± 0.012
S60-300							30	17.30 ± 0.30	0.646 ± 0.004
S60-450							45	15.27 ± 0.17	0.558 ± 0.005
110P8-075	Potter 110P8	0.68	2.8	7.8	16.9	0.173	7.5	22.57 ± 0.39	0.879 ± 0.008
110P8-150							15	21.97 ± 0.55	0.819 ± 0.007
110P8-300							30	19.91 ± 0.32	0.721 ± 0.003
110P8-450							45	18.69 ± 0.25	0.607 ± 0.004

[a] Particle shell thickness (t_s) is measured using SEM images of CPS particles embedded and polished in an epoxy matrix.
[b] Average values and standard deviation of elastic modulus and thermal conductivity from five are reported in the format: (Average value) ± (Standard Deviation).

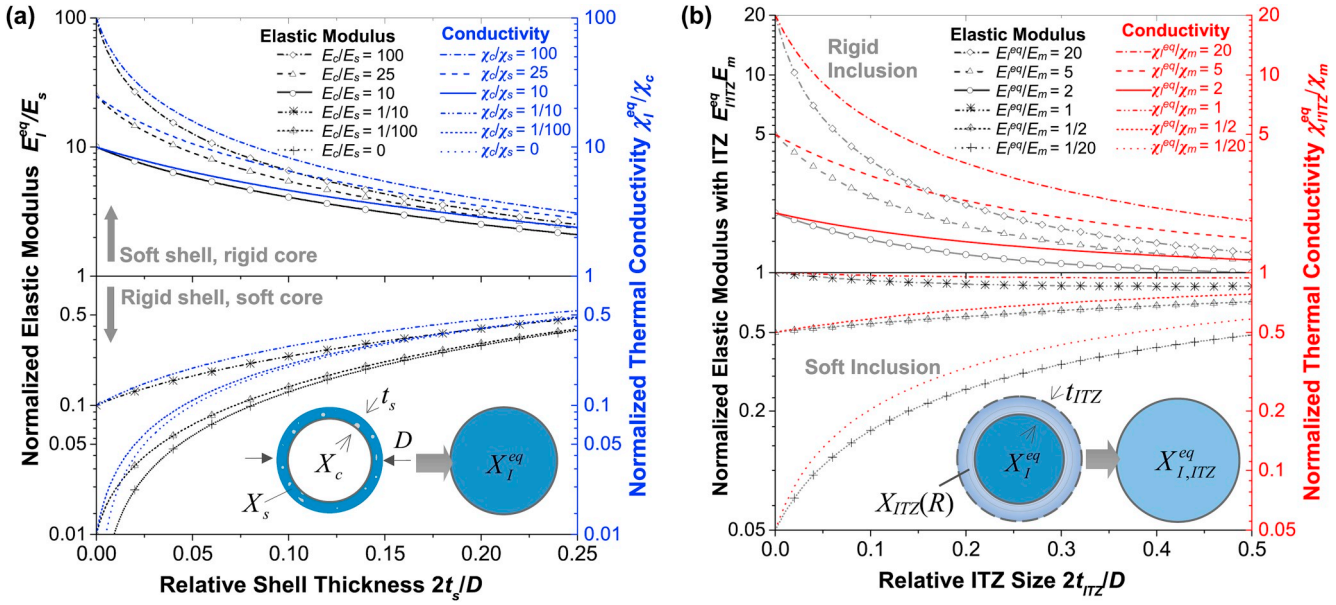

Fig. 7. Equivalence between a CSP and solid particle: (a) normalized equivalent elastic modulus; and (b) equivalent elastic modulus with the consideration of ITZ.

particle and a solid sphere without including the ITZ. Using Equations (1)-(2), the elastic modulus of the equivalent particle, E_I^{eq} (normalized by the elastic modulus of the shell, E_s) is plotted as a function of relative shell thickness, $2t_s/D$. Two different scenarios with $E_c < E_s$ (stiff shell with soft core) and $E_c > E_s$ (stiff core with soft shell) are plotted in Fig. 7 (a). In both cases, results show that the stiffness of the equivalent particle depends largely on the relative shell thickness.

The effect of the interfacial transition zone (ITZ) is considered by Equations (6)–(8). The effective elastic modulus of the embedded CSP with ITZ, $E_{I,ITZ}^{eq}$ (normalized by the elastic modulus of the matrix, E_m), is plotted as a function of the relative thickness of the ITZ layer respective to the particle size, $2t_{ITZ}/D$ in Fig. 7 (b), assuming $E_{ITZ,min} = 0.6E_m$ and $E_I^{eq}/E_m = 2$, 5, 20 (stiff inclusion) (Fig. 7 (b), upper) and $E_I^{eq}/E_m = 1$, 1/2, and 1/20 (soft inclusion) (Fig. 7 (b), lower). As expected, for stiff inclusions ($E_I^{eq} > E_m$), higher ITZ thickness leads to lower normalized stiffness. Overall, $E_{I,ITZ}^{eq}$ is more sensitive to the ITZ thickness for particles that are significantly stiffer than the matrix, e.g., when $E_{I,ITZ}^{eq}/E_m = 20$, the normalized elastic modulus reduces by 75% as $2t_{ITZ}/D$ increases from 0 to 0.1, whereas the amount of reduction is about 26% for particles having effective stiffness comparable to the matrix (i.e., when $E_{I,ITZ}^{eq}/E_m = 2$). $E_{I,ITZ}^{eq}$ becomes relative insensitive to the ITZ size (nor the particle stiffness, E_I^{eq}) when $2t_{ITZ}/D > 0.2$ – i.e., overall properties of the composite system will be dominated by ITZ property when ITZ size is comparable to the inclusion size. For a specified matrix and interface, $2t_{ITZ}/D$ increases as the particle size D decreases which is a source of the size effect. For soft inclusions ($E_I^{eq} < E_m$), the effect of ITZ is relatively moderate.

Similarly, the equivalence of thermal conductivity χ_I^{eq}, between a CSP and a solid particle without and with the consideration of ITZ are plotted as color lines in Fig. 7 (a) and (b), respectively. Again, two scenarios with $\chi_c < \chi_s$ (e.g., hollow particles) and $\chi_c > \chi_s$ (solid particles with non-conductive coating) are plotted. Similar to the elastic modulus, the thermal conductivity of the equivalent particle strongly depends on the relative shell thickness. $\chi_{I,ITZ}^{eq}$ is more sensitive to the ITZ size when there is a large property difference between the inclusion and matrix phases.

5.2. Simulation results and experimental validation

Having found the equivalence between a CSP and an equivalent solid particle, the effective elastic and thermal conductive constants of cementitious composites were then obtained using numerical or analytical homogenization methods. Fig. 8 (a) and (b) plot the effective elastic modulus and effective thermal conductivity (ETC) simulated by finite element approach (FEA), Mori-Tanaka model, and differential effective medium theory (DEMT) [56], as functions of CSP volume fractions in comparison with the experimental test results. The added CSP are hollow particles made of a soda-lime-borosilicate glass shell ($E = 60$ GPa, Poisson's ratio $= 0.21$, $\chi_s = 1.05$ W/m-K) and the cement matrix has a water-cement ratio of 0.28 with air-content of 2%. The air void is assumed to have a spherical shape in the Mori-Tanaka model. Results show that the equivalence relation combined with the FEA homogenization or Mori-Tanaka model agrees well with experimental results, both for effective elastic and thermal conductive properties, see Fig. 8 (a) and (b). It is noted that even at higher CSP volume fractions (i.e., $\varphi > 30\%$), the FEA and Mori-Tanaka predictions are still quite acceptable, whereas other effective medium theories (e.g., DEMT) have been reported to be inaccurate when CPS volume fraction is high [12]. This is because DEMT and GSCM assume small perturbations and do not account for the interactions between particle inclusions [57].

5.3. Effects of CSP particle size, shell thickness, and volume fraction

The effective elastic modulus and thermal conductivity are plotted as functions of the relative shell thickness, $2t_s/D_{50}$, and CSP volume fraction in Fig. 9 (a) and (b). It was noted that when the hollow glass bubble has relative shell thickness, $2t_s/D_{50}$, greater than 0.28, its stiffness including ITZ will exceed that of the matrix and, therefore, becomes a 'stiff' inclusion in the cementitious material. Since the shell wall thickness of most commercially produced micro-size glass bubbles is relative uniform (i.e., 0.8–1.5 μm), adding CSP will not reduce the elastic modulus of the composite if the particle sizes are mostly smaller than ($D_{90} < 10$ μm). On the other hand, since the thermal conductivity of borosilicate glass is similar to that of the cementitious matrix, the ETC of composite will decrease as the CSP volume fraction increases regardless of the relative shell thickness.

5.4. Effects of the Interfacial Transition Zone (ITZ)

As aforementioned, the ITZ has notable impacts on both the elastic and thermal conductive properties of cementitious composites containing micro-size CSP inclusions. Because the median CSP sizes (see Table 1) are close to the size of cement particle (i.e., D_{50} is approximately 30 μm and 5 μm for Portland cement Type I and II respectively [58]), a reduced wall effect is expected to develop around CSP inclusions [59]. In this study, the range (thickness) of the ITZ around CPS particles was set as $0.1D_{50}$, which agrees with the assumption used in Falzone et al.'s study [12]. The volume fraction of the total ITZ regions that forms part of a connected cluster is then computed as a function of the volume fraction of CSP present based on Equation (9). It is also noted that when the CSP volume fraction is high, it is necessary to account for the percolation (overlapping) of ITZ regions when calculating the ITZ volume fraction, φ_{ITZ}. Fig. 10 plots φ_{ITZ} within the composite as a function of the CSP volume fraction, φ, and ITZ thickness t_{ITZ}. The percolation

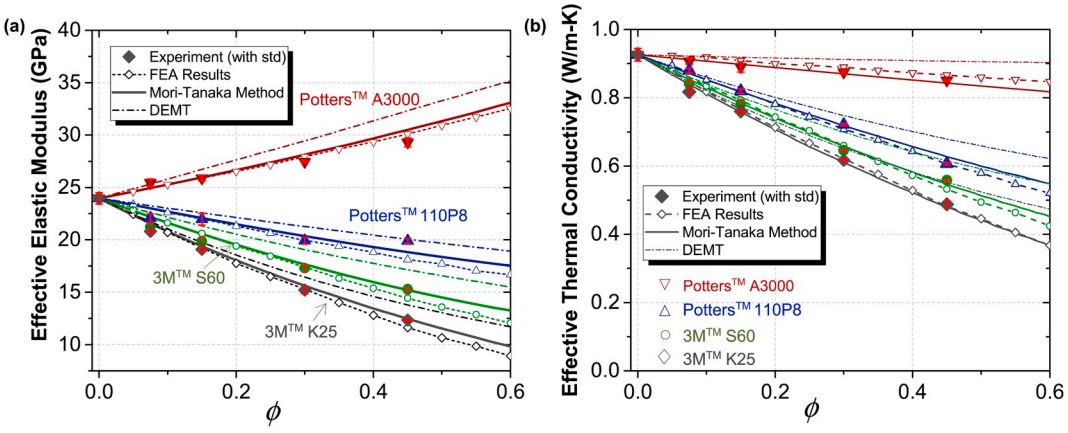

Fig. 8. Effective properties of cementitious composites containing CSP inclusions: (a) effective elastic modulus; and (b) effective thermal conductivity.

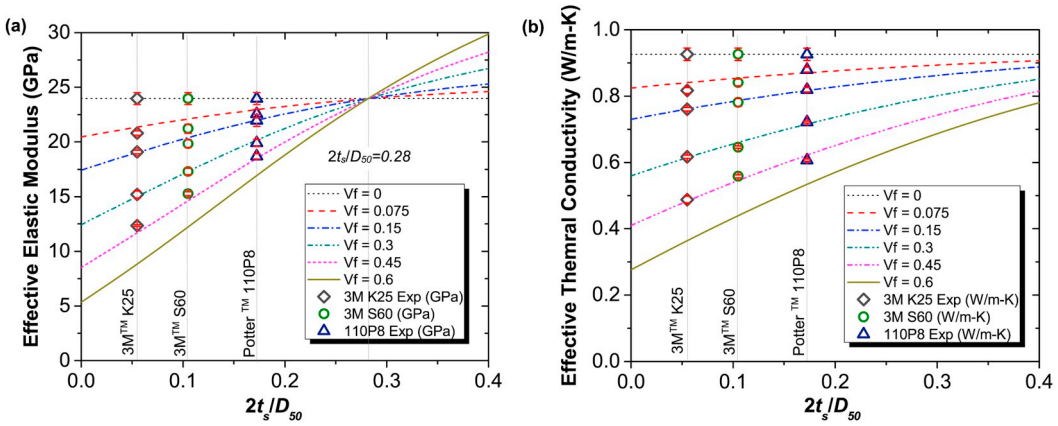

Fig. 9. Effects of CSP relative shell thickness and volume fraction on: (a) effective elastic modulus; and (b) effective thermal conductivity.

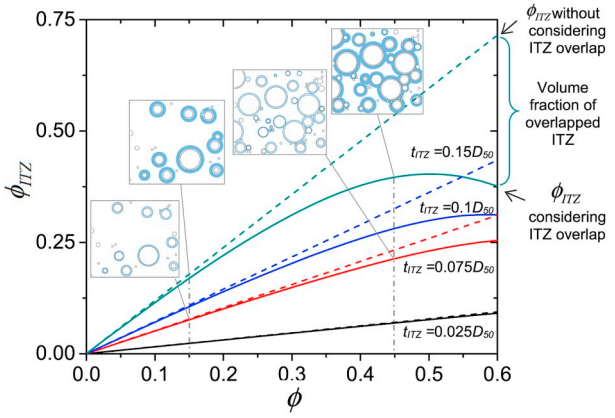

Fig. 10. The effects of percolation (overlap) of ITZ regions within the composites.

(overlapping) effect becomes substantial when $2t_{ITZ}/D_{50}$ is greater than 0.05 for $\varphi > 25\%$, which is generally the case for CSP in the size range of tens of microns or smaller.

5.5. Effects of shell property and particle size distribution

Fig. 11 shows the effective elastic modulus and thermal conductivity plotted as functions of the particle size distribution (i.e., log-normal distribution 1 (L-N-1), log-normal distribution 2 (L-N-2), and mono-size, see Fig. 11 (a)) and CSP shell materials (i.e., borosilicate glass, high-density polyethylene (HDPE), and silica carbide (SiC) ceramic). All particles were assumed to be hollow with the shell thickness 5% of median particle diameter D_{50}. While the effective elastic modulus varies slightly with the distribution pattern of particle size – i.e., with the same median particle diameter (D_{50}) the greater spread particle size led to slightly lower elastic modulus, see Fig. 11 (b). This is mainly attributed to the higher accumulative ITZ volume with the more spread particle size (i.e., the L-N-2) [60]. Particularly, when the relative elastic modulus

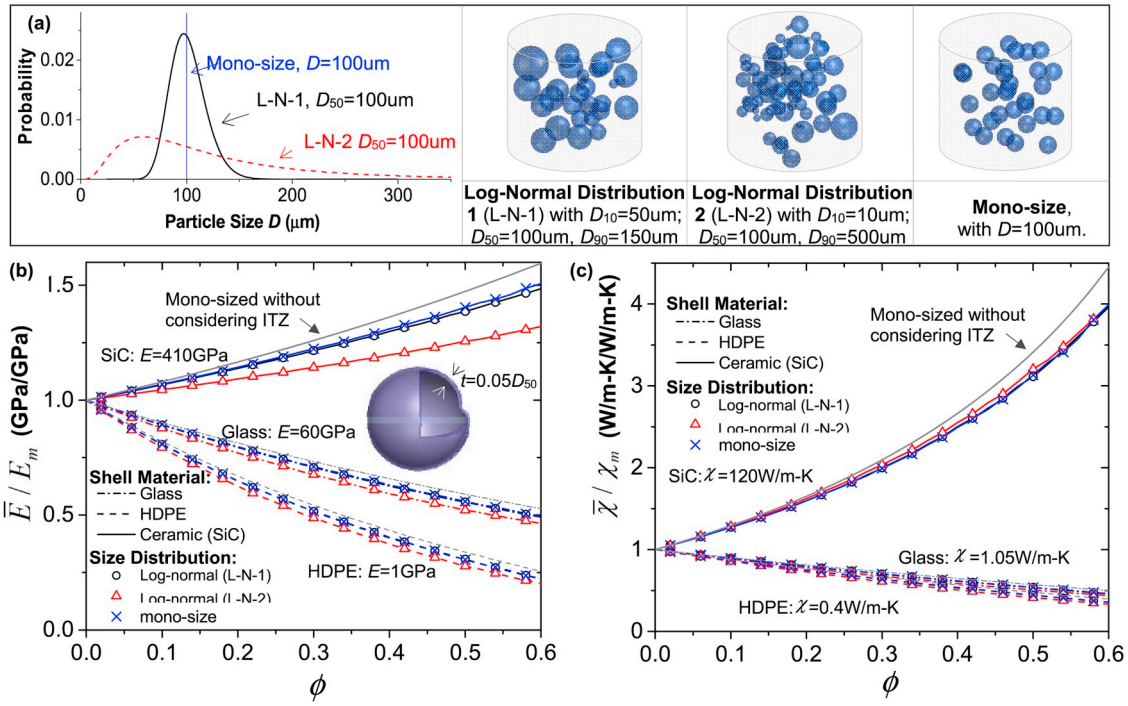

Fig. 11. Effects of shell properties and particle size distribution on the properties of cmentitious composites containing CSP: (a) CSP size distribution; (b) effective elastic modulus; and (c) effective thermal conductivity.

of particle (E_I^{eq}/E_m) is high, the ITZ volume increase would have higher impact on the effective properties of composites (see Fig. 6 (b)) – i.e., for small particles having stiff shell (e.g., SiC CSP with $D < D_{50}$), the equivalent particle stiffness, E_I^{eq}, is much higher than that of the matrix, therefore, the ITZ would have a greater impact on the effective stiffness $E_{I,ITZ}^{eq}$ of CSP in this size range. On the other hand, regardless of the various particle distributions, all the ETC simulation points sit almost perfectly on a curve (Fig. 11 (c)), suggesting that the ETC of cementitious composites is nearly independent of the size distribution and the CSP volume fraction is the main controlling parameter [17].

5.6. Effects of particle shape

So far, the discussion has been mainly limited to spherical inclusions, which is generally the case with most functional core-shell particulate additives. To broaden the scope of the proposed homogenization approach, this section discusses the effects of inclusion shape on the mechanical and thermal properties of the composite system. The effective elastic modulus of cementitious composites containing randomly distributed ellipsoidal inclusions can be simulated using microstructure-guided FEA or using the Mori-Tanaka approach proposed by Hu and Weng [28] for the effective elastic modulus and Stansky et al. [52] for the effective thermal conductivity. Results obtained from finite element simulations and Mori-Tanaka predictions are plotted in Fig. 12 to present the effects of inclusion shape (defined by the aspect ratio $\beta = a{:}c$) on elastic (Fig. 12 (b)) and thermal conductive (Fig. 12 (c)) properties of cementitious composites. These results indicate not only the influence of the shape of inclusions on the macroscopic properties but also a strong dependence of these predictions on the contrast of material properties of individual phases. For both cases with 'stiff' ($X_I^{eq}/X_m = 5$) and 'soft' ($X_I^{eq}/X_m = 0.2$) inclusions, the effective moduli and conductivity of composites with randomly oriented ellipsoidal inclusions always stay within the Hashin-Shtrikman (HS) bounds (indicated by the yellow

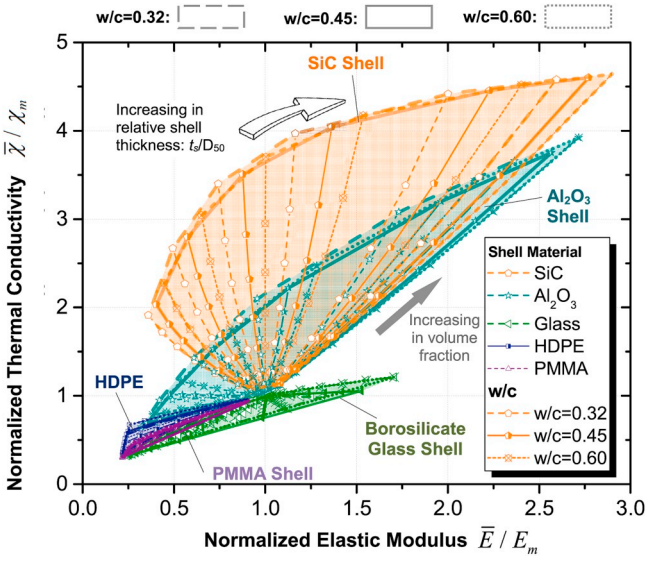

Fig. 13. Material design space for multifunctional cementitious composites.

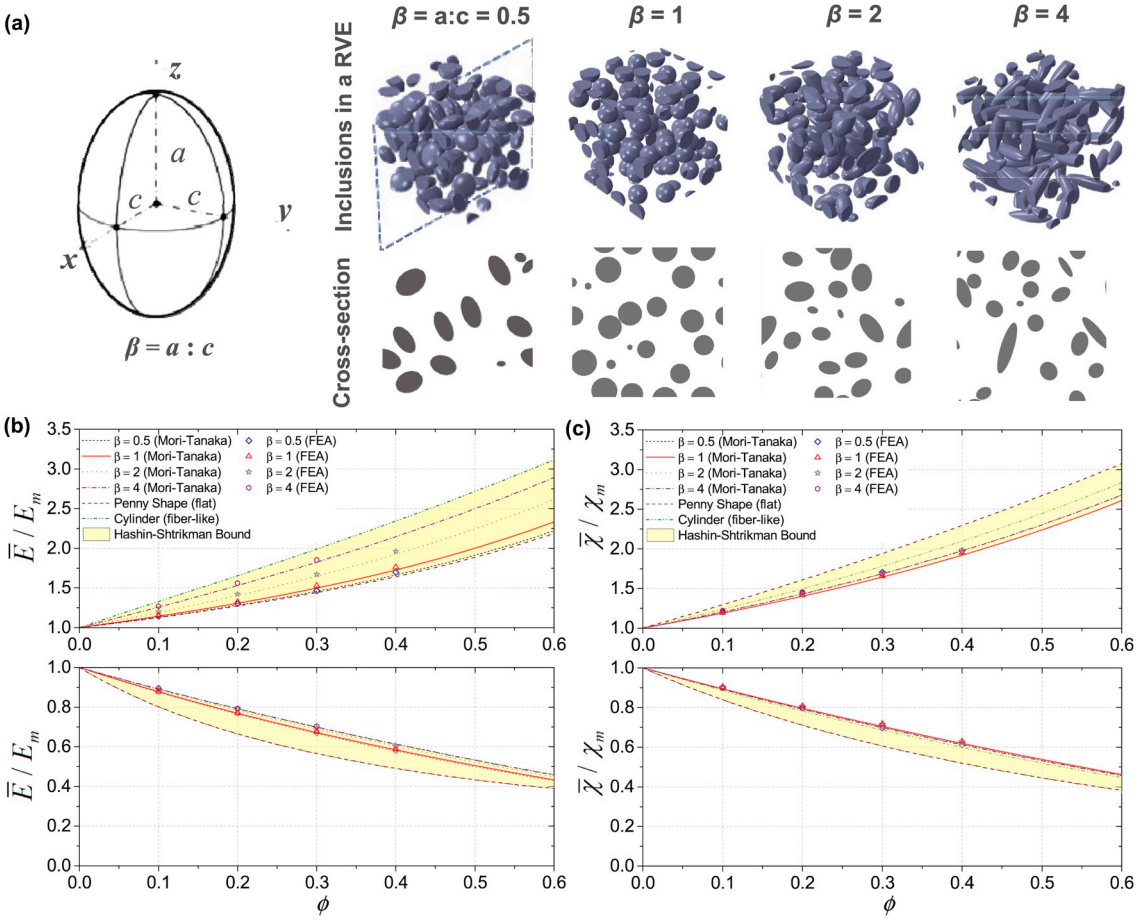

Fig. 12. Influence of particle shape on elastic and thermal properties: (a) different aspect ratios studied herein; the variations of (b) elastic modulus; and (c) thermal conductivity as functions of particle shape.

band). However, the effective elastic modulus of the composite increases as the shape of the inclusions changes from flat disk ('penny-shape') to cylindrical ('fiber-like'); whereas the thermal conductivity is bounded between spherical and penny-shape inclusions, see Fig. 12. For both cases, particle shape has a higher influence on composites with 'stiff' (or more conductive) inclusions than those with 'soft' inclusions.

5.7. Material design space for cementitious composites

In the design of multifunctional cementitious composites, acceptable mechanical properties are often required since the component should have certain stiffness and strength to support loads. The materials property map shown in Fig. 13 is used to visualize the correlations between thermal and mechanical properties of cementitious composites containing CSP additives, where the normalized effective thermal conductivity, $\overline{\chi}/\chi_m$, is plotted against normalized elastic modulus, $\overline{E}/E_m$, for cementitious composites containing CPS with varying shell materials, relative shell thicknesses, and volume fraction. Three categories and a total of five types of shell material (ceramics: SiC, alumina ($A1_2O_3$), glass, and polymers: HDPE and Poly methyl methacrylate (PMMA)) are plotted with $2t_s/D_{50}$ varying from 0.005 to 0.2 (following the tangential direction in Fig. 13). The effective thermal conductivity and elastic modulus predictions are calculated with the CPS volume fraction varying between $0.5\% < \phi < 60\%$ (volume fraction increases following the radial direction in Fig. 13). In addition, three different water-to-cement ratios are considered in the simulation (i.e., w/c = 0.32, w/c = 0.45, w/c = 0.60). The results show a very wide design space of cementitious composites enabled by varying materials, relative thicknesses, and volume fractions. Such a wide design space, together with the further design of shell porosity and surface coating [61], makes hollow and core-shell particulate materials very versatile and promising functional additives for cement-based materials. Our recent studies [4,5] show that by using hollow spheres with stiff shell and higher relative shell thickness (thicker shell or smaller size), low-density and low thermal conductivity cementitious composites can be designed with acceptable mechanical properties. Studies conducted by Wang et al. [13] also indicated that by encapsulating soft phase-changing material (PCM) – e.g., Paraffin wax, in hard and stiff shells (fly-ash cenosphere), the strength and stiffness loss posed by traditional PCM encapsulation technology can be largely circumvented.

6. Conclusions

In this work, we have presented a micromechanical model that accurately predicts the effective elastic and thermal properties of cementitious composites containing hollow and core-shell particulate (CSP) functional additives. The proposed model utilizes a two-stage homogenization scheme: the properties of CSP, including the surrounding interfacial transition zone (ITZ), are equivalently represented by a solid particle of the same size; then the effective properties of the composite system are obtained through numerical (i.e., finite element) or analytical (Mori-Tanaka) homogenization methods. It takes advantages of the models previously developed for solid particle filled composites; thus, it is easy to use and versatile. The effective elastic modulus and thermal conductivity predicted by the proposed model are experimentally validated, showing that the model provides accurate property prediction of functional cementitious composites with different CPS volume fraction, core- (and shell) material type, and particle size.

More importantly, this work provides insights into the design of functional cementitious composites through parametric studies. A scoping study was carried out to investigate the effects of varying CSP particle size (relative shell thickness), volume fraction, as well as shell properties to provide guidelines for the design and selection of micro-size CSP additives for cementitious composite materials. Furthermore, the effects of CSP size distribution and packing pattern are also investigated. Aside from the well-known key parameters such as relative shell thickness and CSP volume fraction, the range of interfacial transition zone (ITZ) and its varying properties have significant impacts on both the elastic and thermal properties of cementitious composites containing micro- and nano-size CSP additives. Thus, future study on the range (thickness) and property variation within the ITZ around micro- and nano-size particles are of great importance for the design of functional cementitious composites.

Declaration of competing interest

The authors declare no conflict of interest (COI).

Acknowledgements

This research is partially sponsored by the U.S. Department of Energy (DE-EE-0008677) and the National Science Foundation (NSF CMMI-1663302). The funding supports from DOE and NSF are greatly appreciated. The authors would like to thank Mr. Adam Brooks for conducting the validation experiments and Dr. Mansoureh Norouzi Rad from Carl Zeiss Microscopy for performing the X-ray microtomography (XRM) analysis.

Appendix A. Equivalent thermal conductivity of core-shell particle with interfacial contact resistance between core and shell

The temperature distribution is defined by steady-state heat conduction in a spherical coordinate (R, θ, γ), see Fig. A.1, as:

$$\nabla^2 T_n = \frac{1}{R^2}\frac{\partial}{\partial R}\left(R^2\frac{\partial T_n}{\partial R}\right) + \frac{1}{R^2\sin\theta}\frac{\partial}{\partial\theta}\left(\sin\theta\frac{\partial T_n}{\partial\theta}\right) = 0 \tag{A.1}$$

where T_n is the temperature of the nth phase, i.e., the effective medium (eq), core (c), and shell (s).

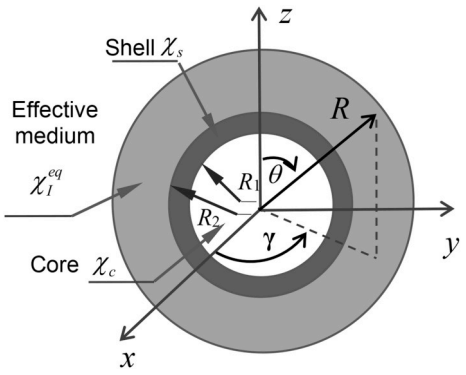

Fig. A.1. Effective medium field analysis of core/shell particle

The general solution of Equation (A.1) may be written as:

$$T_n(R,\theta) = \left(F_n R + G_n / R^2\right)\cos\theta \tag{A.2}$$

where F_n and G_n are coefficients which can be determined by the boundary conditions and the interface continuity conditions.

Apply far-field temperature boundary condition [62]:

$$\lim_{R\to\infty} T_0(R,\theta) = -H_{eq} z = -H_{eq} R\cos\theta \tag{A.3}$$

where H_{eq} is the temperature gradient in the effective medium. The far-field boundary condition ($R\to\infty$) requires $F_{eq} = -H_{eq}$, and the solution at $R = 0$ is finite leads to $G_c = 0$. The remaining four coefficients, i.e., F_c, F_s, G_{eq} and G_s are determined by the interface continuity conditions of heat flux and temperature. At $R = R_1$, the heat flux continuity yields:

$$-\chi_c \frac{dT_c(R,\theta)}{dR} = -\chi_s \frac{dT_s(R,\theta)}{dR} \tag{A.4}$$

Due to the existence of contact resistance at the interface of the core and shell, the temperature may not be continuous, therefore:

$$-\chi_c \frac{dT_c(R,\theta)}{dR} = \frac{1}{h_{cs}}\left[T_c(R,\theta) - T_s(R,\theta)\right] \tag{A.5}$$

where h_{cs} is the interface contact conductance between the core and shell.

Since the particle is assumed to be embedded in the effective medium that resemble the effective property of the particle, at $R = R_2$, the continuity of the heat flux and temperature yields:

$$-\chi_s \frac{dT_s(R,\theta)}{dR} = -\chi_1^{eq} \frac{dT_{eq}(R,\theta)}{dR} \tag{A.6}$$

$$T_s(R,\theta) = T_{eq}(R,\theta) \tag{A.7}$$

The equivalent thermal conductivity is evaluated as (due to symmetry, only the averaged z-components are non-zero):

$$\chi_1^{eq} = \overline{q}_z / \overline{H}_z \tag{A.8}$$

where, q_z is the heat flux, and the overbar represents the volumetric average, i.e., $\overline{m} = (1/V)\int_V m dV$, over the core/shell particle with $V = (4\pi R_2^3/3)$.

The volumetric average heat flux is:

$$\overline{q}_z = \overline{q}_{z,c} p + \overline{q}_{z,s}(1-p) \tag{A.9}$$

with $\overline{q}_{z,c} = \lambda_c \overline{H}_{z,c}$, and $\overline{q}_{z,s} = \lambda_s \overline{H}_{z,s}$; and p=(R_1^3/R_2^3) is the volume fraction of the core. The volumetric average temperature gradient is:

$$\overline{H}_z = \overline{H}_{z,c} p + \overline{H}_{z,s}(1-p) + J_{cs} f \tag{A.10}$$

where, $f = (1 + t_s/R_1)^{-3}$, $t_s = R_2 - R_1$, and $J_{cs} = (F_c - F_s) + (G_c - G_s)/R_1^3$ fis the temperature gradient caused by temperature discontinuity at the interface between the core and shell.

The temperature gradients of the nth phase, $H_{z,n}$, is calculated as:

$$-H_{z,n} = \frac{\partial T_n}{\partial z} = F_n - \frac{\sin^2\theta - 2\cos^2\theta}{R^3} G_n \tag{A.11}$$

Then, the volumetric average of $H_{z,n}$ of the nth phase is obtained as:

$$\overline{H}_n = -F_n \tag{A.12}$$

Thus, solving Equation (A.4) – (A.7) for coefficients F_c, F_s, G_{eq} and G_s, then substitute Equation (A.9), (A.10), (A.12) into (A.8), it yields:

$$\chi_I^{eq} = \frac{2(1-f)\chi_s\chi_c + (2(1-f)\chi_s + (1+2f)\chi_c)(R_1/h_{cs})}{(2+f)\chi_s\chi_c + ((2+f)\chi_s + (1-f)\chi_c)(R_1/h_{cs})}\chi_s \tag{A.13}$$

References

[1] X. Huang, R. Ranade, Q. Zhang, W. Ni, V.C. Li, Mechanical and thermal properties of green lightweight engineered cementitious composites, Constr. Build. Mater. 48 (2013) 954–960, https://doi.org/10.1016/j.conbuildmat.2013.07.104.

[2] A. Hanif, Z. Lu, Y. Cheng, S. Diao, Z. Li, Effects of different lightweight functional fillers for use in cementitious composites, Int J Concr Struct Mater 11 (2017) 99–113, https://doi.org/10.1007/s40069-016-0184-1.

[3] A. Hanif, Z. Lu, Z. Li, Utilization of fly ash cenosphere as lightweight filler in cement-based composites – a review, Constr. Build. Mater. 144 (2017) 373–384, https://doi.org/10.1016/j.conbuildmat.2017.03.188.

[4] A.L. Brooks, H. Zhou, D. Hanna, Comparative study of the mechanical and thermal properties of lightweight cementitious composites, Constr. Build. Mater. 159 (2018) 316–328, https://doi.org/10.1016/j.conbuildmat.2017.10.102.

[5] H. Zhou, A.L. Brooks, Thermal and mechanical properties of structural lightweight concrete containing lightweight aggregates and fly-ash cenospheres, Constr. Build. Mater. 198 (2019) 512–526, https://doi.org/10.1016/j.conbuildmat.2018.11.074.

[6] S.E. Kalnaes, B.P. Jelle, Phase change materials and products for building applications: a state-of-the-art review and future research opportunities, Energy Build. 94 (2015) 150–176, https://doi.org/10.1016/j.enbuild.2015.02.023.

[7] Y. Konuklu, M. Ostry, H.O. Paksoy, P. Charvat, Review on using microencapsulated phase change materials (PCM) in building applications, Energy Build. 106 (2015) 134–155, https://doi.org/10.1016/j.enbuild.2015.07.019.

[8] K. Vijay, M. Murmu, S.V. Deo, Bacteria based self healing concrete – a review, Constr. Build. Mater. 152 (2017) 1008–1014, https://doi.org/10.1016/j.conbuildmat.2017.07.040.

[9] J. Gilford, M.M. Hassan, T. Rupnow, M. Barbato, A. Okeil, S. Asadi, Dicyclopentadiene and sodium silicate microencapsulation for self-healing of concrete, J. Mater. Civ. Eng. 26 (2014) 886–896, https://doi.org/10.1061/(ASCE)MT.1943-5533.0000892.

[10] A. Ricklefs, A.M. Thiele, G. Falzone, G. Sant, L. Pilon, Thermal conductivity of cementitious composites containing microencapsulated phase change materials, Int. J. Heat Mass Transf. 104 (2017) 71–82, https://doi.org/10.1016/j.ijheatmasstransfer.2016.08.013.

[11] B.A. Young, A.M. Fujii, A.M. Thiele, A. Kumar, G. Sant, E.P.L. Taciroglu, B. A. Young, A.M.K. Fujii, A.M. Thiele, A. Kumar, G. Sant, et al., Effective elastic moduli of core-shell-matrix composites, Mech. Mater. 92 (2016) 94–106, https://doi.org/10.1016/j.mechmat.2015.09.006.

[12] G. Falzone, G.P. Falla, Z. Wei, M. Zhao, A. Kumar, M. Bauchy, et al., The influences of soft and stiff inclusions on the mechanical properties of cementitious composites, Cement Concr. Compos. 71 (2016) 153–165, https://doi.org/10.1016/j.cemconcomp.2016.05.008.

[13] F. Liu, J. Wang, X. Qian, Integrating phase change materials into concrete through microencapsulation using cenospheres, Cement Concr. Compos. 80 (2017) 317–325, https://doi.org/10.1016/j.cemconcomp.2017.04.001.

[14] S. Das, M. Aguayo, S.D. Rajan, G. Sant, N. Neithalath, Microstructure-guided numerical simulations to predict the thermal performance of a hierarchical cement-based composite material, Cement Concr. Compos. 87 (2018) 20–28, https://doi.org/10.1016/j.cemconcomp.2017.12.003.

[15] E. Ghossein, M. Lévesque, A comprehensive validation of analytical homogenization models: the case of ellipsoidal particles reinforced composites, Mech. Mater. 75 (2014) 135–150, https://doi.org/10.1016/j.mechmat.2014.03.014.

[16] E.J. Garboczi, D.P. Bentz, Analytical formulas for interfacial transition zone properties, Adv. Cem. Base Mater. 6 (1997) 99–108.

[17] A.M. Thiele, A. Kumar, G. Sant, L. Pilon, Effective thermal conductivity of three-component composites containing spherical capsules, Int. J. Heat Mass Transf. 73 (2014) 177–185, https://doi.org/10.1016/j.ijheatmasstransfer.2014.02.002.

[18] J.D. Eshelby, The determination of the elastic field of an ellipsoidal inclusion and related problems, Proc R Soc A 241 (1957) 376–396.

[19] R. Hill, A self-consistent mechanics of composite materials, J. Mech. Phys. Solids 13 (1965) 213–222, https://doi.org/10.1016/0022-5096(65)90010-4.

[20] Z. Hashin, The elastic moduli of heterogeneous materials, J. Appl. Mech. 29 (1962) 143–150.

[21] R.M. Christensen, K.H. Lo, Solutions for effective shear properties in three phase sphere and cylinder models, J. Mech. Phys. Solids 27 (1979) 315–330, https://doi.org/10.1016/0022-5096(79)90032-2.

[22] Y. Huang, K.C. Hwang, K.X. Hu, A. Chandra, A unified energy approach to a class of micromechanics models for composite materials, Acta Mech. Sin. 11 (1995) 59–75.

[23] R. Mclaughlin, A study of the differential scheme for composite materials, Int. J. Eng. Sci. 15 (1977) 237–244.

[24] A.N. Norris, A.J. Callegari, P. Sheng, A generalized differential effective medium theory, J. Mech. Phys. Solids 33 (1985) 525–543, https://doi.org/10.1016/0022-5096(85)90001-8.

[25] T. Mori, K. Tanaka, Average stress in matrix and average elastic energy of materials with misfitting inclusions, Acta Metall. 21 (1973) 571–574, https://doi.org/10.1016/0001-6160(73)90064-3.

[26] A.N. Norris, An examination of the mori-tanaka effective medium approximation for multiphase composites, J. Appl. Mech. 56 (1989) 83, https://doi.org/10.1115/1.3176070.

[27] G.J. Weng, The theoretical connection between Mori-Tanaka's theory and the Hashin-Shtrikman-Walpole, Int. J. Eng. Sci. 28 (1990) 1111–1120.

[28] G.K. Hu, G.J. Weng, Some reflections on the Mori-Tanaka and Ponte Castaneda-Willis methods with randomly oriented ellipsoidal inclusions, Acta Mech. 140 (2000) 31–40, https://doi.org/10.1007/BF01175978.

[29] W.R.L. Da Silva, J. Němeček, P. Štemberk, Methodology for nanoindentation-assisted prediction of macroscale elastic properties of high performance cementitious composites, Cement Concr. Compos. 45 (2014) 57–68, https://doi.org/10.1016/j.cemconcomp.2013.09.013.

[30] G. Constantinides, F.J. Ulm, The effect of two types of C-S-H on the elasticity of cement-based materials: results from nanoindentation and micromechanical modeling, Cement Concr. Res. 34 (2004) 67–80, https://doi.org/10.1016/S0008-8846(03)00230-8.

[31] R. Davies, A. Jefferson, Micromechanical modelling of self-healing cementitious materials, Int. J. Solids Struct. 113–114 (2017) 180–191, https://doi.org/10.1016/j.ijsolstr.2017.02.008.

[32] Y. Ke, S. Ortola, a. L. Beaucour, H. Dumontet, Identification of microstructural characteristics in lightweight aggregate concretes by micromechanical modelling including the interfacial transition zone (ITZ), Cement Concr. Res. 40 (2010) 1590–1600, https://doi.org/10.1016/j.cemconres.2010.07.001.

[33] K. Miled, O. Limam, Effective thermal conductivity of foam concretes: homogenization schemes vs experimental data and FEM simulations, Mech. Res. Commun. 76 (2016) 96–100, https://doi.org/10.1016/j.mechrescom.2016.07.004.

[34] M. Aguayo, S. Das, C. Castro, N. Kabay, G. Sant, N. Neithalath, Porous inclusions as hosts for phase change materials in cementitious composites: characterization, thermal performance, and analytical models, Constr. Build. Mater. 134 (2017) 574–584, https://doi.org/10.1016/j.conbuildmat.2016.12.185.

[35] A. Eddhahak-Ouni, S. Drissi, J. Colin, J. Neji, S. Care, Experimental and multi-scale analysis of the thermal properties of Portland cement concretes embedded with microencapsulated Phase Change Materials (PCMs), Appl. Therm. Eng. 64 (2014) 32–39, https://doi.org/10.1016/j.applthermaleng.2013.11.050.

[36] J. Vorel, V. Šmilauer, Z. Bittnar, Multiscale simulations of concrete mechanical tests, J. Comput. Appl. Math. 236 (2012) 4882–4892, https://doi.org/10.1016/j.cam.2012.01.009.

[37] S. Das, A. Maroli, S.S. Singh, T. Stannard, X. Xiao, N. Chawla, et al., A microstructure-guided constitutive modeling approach for random heterogeneous materials: application to structural binders, Comput. Mater. Sci. 119 (2016) 52–64, https://doi.org/10.1016/j.commatsci.2016.03.040.

[38] J.D. Eshelby, The continuum theory of lattice defects, Solid State Phys - Adv Res Appl 3 (1956) 79–144, https://doi.org/10.1016/S0081-1947(08)60132-0.

[39] Z. Jia, Z. Wang, D. Hwang, L. Wang, Prediction of the effective thermal conductivity of hollow sphere foams, ACS Appl. Energy Mater. 1 (2018) 1146–1157, https://doi.org/10.1021/acsaem.7b00264.

[40] M.P. Lutz, P.J.M. Monteiro, R.W. Zimmerman, Inhomogeneous interfacial transition zone model for the bulk modulus of mortar, Cement Concr. Res. 27 (1997) 1113–1122.

[41] J. Hu, P. Stroeven, Properties of the interfacial transition zone in model concrete, Interface Sci. 12 (2004) 389–397, https://doi.org/10.1023/B:INTS.0000042337.39900.fb.

[42] P. Stroeven, M. Stroeven, Reconstructions by SPACE of the interfacial transition zone, Cement Concr. Compos. 23 (2001) 189–200, https://doi.org/10.1016/S0958-9465(00)00076-7.

[43] I. Sevostianov, M. Kachanov, Effect of interphase layers on the overall elastic and conductive properties of matrix composites. Applications to nanosize inclusion, Int. J. Solids Struct. 44 (2007) 1304–1315, https://doi.org/10.1016/j.ijsolstr.2006.06.020.

[44] L. Shen, J.J. Li, Effective elastic moduli of composites reinforced by particle or fiber with an inhomogeneous interphase, Int. J. Solids Struct. 40 (2003) 1393–1409, https://doi.org/10.1016/S0020-7683(02)00659-5.

[45] L. Shen, J. Li, Homogenization of a fibre/sphere with an inhomogeneous interphase for the effective elastic moduli of composites, Proc. R. Soc. A Math. Phys. Eng. Sci. 461 (2005) 1475–1504, https://doi.org/10.1098/rspa.2005.1447.
[46] B. Lu, S. Torquato, Nearest-surface distribution functions for polydispersed particle systems, Phys. Rev. A 45 (1992) 5530–5544, https://doi.org/10.1139/p67-314.
[47] J. Zheng, X. Zhou, X. Jin, An n-layered spherical inclusion model for predicting the elastic moduli of concrete with inhomogeneous ITZ, Cement Concr. Compos. 34 (2012) 716–723, https://doi.org/10.1016/j.cemconcomp.2012.01.011.
[48] S. Das, M. Aguayo, S.D. Rajan, G. Sant, N. Neithalath, Microstructure-guided numerical simulations to predict the thermal performance of a hierarchical cement-based composite material, Cement Concr. Compos. 87 (2018) 20–28, https://doi.org/10.1016/j.cemconcomp.2017.12.003.
[49] B.D. Lubachevsky, F.H. Stillinger, Geometric properties of random disk packings, J. Stat. Phys. 60 (1990) 561–583, https://doi.org/10.1007/BF01025983.
[50] P. Suquet, Elements of homogenization for liner elastic solid mechanics, in: E. Sanchez-Palencia, A. Zaoui (Eds.), Homog. Tech. Compos. Media, Springer, 1987.
[51] B. Klusemann, B. Svendsen, Homogenization methods formulti-phase elastic composites: comparisons and benchmarks, Tech. Mech. 30 (2010) 374–386.
[52] J. Stránský, J. Vorel, J. Zeman, M. Šejnoha, Mori-tanaka based estimates of effective thermal conductivity of various engineering materials, Micromachines 2 (2011) 129–149, https://doi.org/10.3390/mi2020129.
[53] S.E. Gustafsson, Transient diffusivity plane source techniques for thermal conductivity measurements of solid materials and thermal, Rev. Sci. Instrum. 62 (1991) 797–804.
[54] ISO22007-2:2008, Plastics - Determination of Thermal Conductivity and Thermal Diffusivity - Part 2: Transient Plane Source Method, 2008.
[55] Y. He, Rapid thermal conductivity measurement with a hot disk sensor: Part 1. Theoretical considerations, Thermochim. Acta 436 (2005) 122–129, https://doi.org/10.1016/j.tca.2005.06.026.
[56] S. Torquato, Random heterogeneous media: microstructure and improved bounds on effective properties, Appl. Mech. Rev. 44 (1991) 37, https://doi.org/10.1115/1.3119494.
[57] P. Vieville, A.S. Bonnet, P. Lipiński, Modelling effective properties of composite materials using the inclusion concept. General considerations, Arch. Mech. 58 (2006) 207–239, https://doi.org/10.1039/c8cp01029c.
[58] D.P. Bentz, E.J. Garboczi, Effects of cement particle size distribution on performance properties of portland, Cement-Based Materials 8846 (1999) 1663–1671, https://doi.org/10.1016/S0008-8846(99)00163-5.
[59] A. Elsharief, M.D. Cohen, J. Olek, Influence of aggregate size, water cement ratio and age on the microstructure of the interfacial transition zone, Cement Concr. Res. 33 (2003) 1837–1849, https://doi.org/10.1016/S0008-8846(03)00205-9.
[60] S. Das, A. Maroli, N. Neithalath, Finite element-based micromechanical modeling of the influence of phase properties on the elastic response of cementitious mortars, Constr. Build. Mater. 127 (2016) 153–166, https://doi.org/10.1016/j.conbuildmat.2016.09.153.
[61] Z. Jia, Z. Wang, D. Hwang, L. Wang, Prediction of the effective thermal conductivity of hollow sphere foams, ACS Appl. Energy Mater. 1 (2018) 1146–1157, https://doi.org/10.1021/acsaem.7b00264.
[62] J.D. Felske, Effective thermal conductivity of composite spheres in a continuous medium with contact resistance, Int. J. Heat Mass Transf. 47 (2004) 3453–3461, https://doi.org/10.1016/j.ijheatmasstransfer.2004.01.013.